Enhanced antibacterial activity through the controlled alignment of graphene oxide nanosheets

Xinglin Lu[a,1], Xunda Feng[a,1], Jay R. Werber[a], Chiheng Chu[a], Ines Zucker[a], Jae-Hong Kim[a], Chinedum O. Osuji[a], and Menachem Elimelech[a,2]

[a]Department of Chemical and Environmental Engineering, Yale University, New Haven, CT 06520-8286

Edited by Pedro J. J. Alvarez, Rice University, Houston, TX, and accepted by Editorial Board Member Thomas E. Mallouk September 26, 2017 (received for review June 18, 2017)

The cytotoxicity of 2D graphene-based nanomaterials (GBNs) is highly important for engineered applications and environmental health. However, the isotropic orientation of GBNs, most notably graphene oxide (GO), in previous experimental studies obscured the interpretation of cytotoxic contributions of nanosheet edges. Here, we investigate the orientation-dependent interaction of GBNs with bacteria using GO composite films. To produce the films, GO nanosheets are aligned in a magnetic field, immobilized by cross-linking of the surrounding matrix, and exposed on the surface through oxidative etching. Characterization by small-angle X-ray scattering and atomic force microscopy confirms that GO nanosheets align progressively well with increasing magnetic field strength and that the alignment is effectively preserved by cross-linking. When contacted with the model bacterium *Escherichia coli*, GO nanosheets with vertical orientation exhibit enhanced antibacterial activity compared with random and horizontal orientations. Further characterization is performed to explain the enhanced antibacterial activity of the film with vertically aligned GO. Using phospholipid vesicles as a model system, we observe that GO nanosheets induce physical disruption of the lipid bilayer. Additionally, we find substantial GO-induced oxidation of glutathione, a model intracellular antioxidant, paired with limited generation of reactive oxygen species, suggesting that oxidation occurs through a direct electron-transfer mechanism. These physical and chemical mechanisms both require nanosheet penetration of the cell membrane, suggesting that the enhanced antibacterial activity of the film with vertically aligned GO stems from an increased density of edges with a preferential orientation for membrane disruption. The importance of nanosheet penetration for cytotoxicity has direct implications for the design of engineering surfaces using GBNs.

graphene oxide | magnetic alignment | enhanced antibacterial activity | cytotoxicity mechanism | edge-mediated effect

Graphene is a 2D nanomaterial comprising sp^2-bonded carbons arranged in a hexagonal lattice (1). The unique structure of 2D nanomaterials can result in extraordinary physicochemical properties, enabling technical solutions to address global challenges in medicine, water scarcity, and energy production (2). Graphene-based nanomaterials (GBNs), in particular, have attracted substantial research interest over the past decade because of their exceptional mechanical, electronic, and thermal properties (3).

The cytotoxic properties of GBNs are also important due to potential ecological impact and usage in engineered (e.g., antibacterial) applications. Previous studies have demonstrated that GBNs are cytotoxic toward a variety of cell types [e.g., bacterial (4), mammalian (5)] and viruses (6). This cytotoxicity of GBNs has been ascribed to two major mechanisms: physical disruption and chemical oxidation. For physical disruption, previous studies have suggested that GBNs can penetrate into the cell membrane (7, 8), possibly compromising membrane integrity through the formation of pores (9) or through the extraction of lipid molecules (10). The loss of membrane integrity leads to leakage of cytoplasmic compounds [e.g., RNA (4), intracellular electrolyte (6)], which, in turn, causes cell death. For chemical oxidation, GBNs mediate oxidative stress on the cellular membrane, either through the generation of reactive oxygen species (ROS) or through direct electron transfer, thereby oxidizing cellular components (e.g., lipids, proteins) and inactivating viable cells (11, 12). In the past decade, the cytotoxicity of GBNs has been harnessed to mitigate biofouling on engineered surfaces (13–16). For example, GBNs were successfully attached to surfaces through chemical bonding (13, 17) or filter-assisted deposition (16), thereby imparting the surface with enhanced biofouling resistance.

Further investigations into the physical and chemical mechanisms of GBN-induced cytotoxicity highlight the potentially significant contribution of edge effects. For example, modeling results suggest that graphene nanosheets readily penetrate cell membranes when interacting with cells in an orthogonal orientation; at this orientation, the sharp edges possess the lowest energy barrier to initiate local penetration through the lipid bilayer (7). Additionally, the edges of carbon materials could serve as active sites for redox reactions due to the abundance of edge-bound defect sites (12, 18–20). Combined, these properties suggest that the alignment of nanosheets on engineered surfaces may impact the overall antibacterial activity. However, due to the lack of an efficient technique to align GBNs, previous antibacterial surfaces were mainly achieved with uncontrolled nanosheets (13, 16, 17). As such, the effects of nanosheet alignment predicted by modeling have not been experimentally confirmed.

Significance

In biomedical and environmental applications, as well as manufacture and disposal, the interaction of graphene-based nanomaterials (GBNs) with living cells is inevitable and sometimes crucial. While the cytotoxic properties of GBNs are well established, the mechanisms behind the cytotoxicity remain controversial. In this study, we first utilize a magnetic field to form films with aligned graphene oxide (GO), showing that the alignment of sharp GO edges plays a crucial role in the antibacterial activity. We then demonstrate using model systems that GO unequivocally induces physical disruption of lipid bilayers and that oxidation stems from a direct electron transfer mechanism. Altogether, our results elucidate the physicochemical, edge-based cytotoxicity of GBNs, while providing guidance for the design of engineered surfaces using GBNs.

Author contributions: X.L., X.F., and M.E. designed research; X.L., X.F., J.R.W., C.C., and I.Z. performed research; X.L., X.F., J.R.W., C.C., J.-H.K., C.O.O., and M.E. analyzed data; and X.L., X.F., J.R.W., and M.E. wrote the paper.

The authors declare no conflict of interest.

This article is a PNAS Direct Submission. P.J.J.A. is a guest editor invited by the Editorial Board.

[1]X.L. and X.F. contributed equally to this work.

[2]To whom correspondence should be addressed. Email: menachem.elimelech@yale.edu.

This article contains supporting information online at www.pnas.org/lookup/suppl/doi:10.1073/pnas.1710996114/-/DCSupplemental.

Magnetic alignment may provide a powerful tool toward this aim. Recent studies have demonstrated successful magnetic alignment of graphene oxide (GO) (21, 22), an oxidized form of graphene with improved dispersity in a variety of solvents (23). Individual GO nanosheets are alignable due to the additive magnetic anisotropies of the aromatic rings, which are sufficient to overcome thermal disordering effects (24, 25). The diamagnetic anisotropy and solution processability of GO create the possibility to fabricate an engineered surface with nanosheets under controlled orientations.

In this study, we investigate the orientation-dependent interaction of GBNs with bacteria using GO composite films (Fig. 1*A*), in which the GO nanosheets are aligned by a magnetic field and exposed on the surface with different orientations (Fig. 1*B*). When contacted with a model bacterium, *Escherichia coli*, GO nanosheets with vertical orientation exhibit enhanced antibacterial activity compared with random and horizontal orientations. To explain the enhanced antibacterial activity of the Vertical-GO film, we assess the properties of dispersed GO nanosheets using lipid vesicles and chemical probes. Our results indicate that the toxicity of GO nanosheets has combined physical and chemical contributions, with the enhanced antibacterial activity of the Vertical-GO film likely stemming from an increased density of edges with a preferential orientation for membrane disruption.

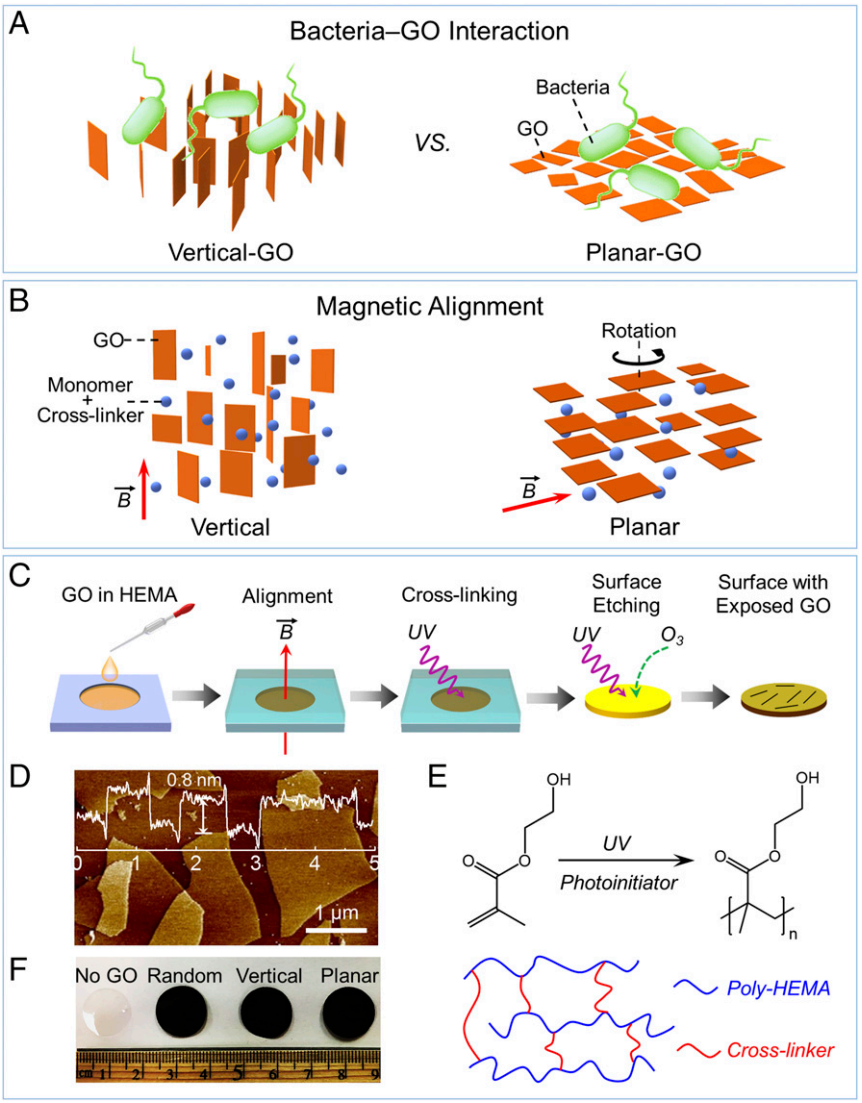

Fig. 1. Fabrication of GO composite films with the controlled orientation of exposed GO nanosheets for antibacterial evaluation. (*A*) Bacterial interaction with different alignment of GO nanosheets. (*B*) Schematic of magnetic response of GO nanosheets. (*Left*) GO nanosheets, which possess a positive diamagnetic susceptibility, align parallel to the magnetic field $\vec{B}$ such that the normal of each nanosheet is degenerately distributed in the plane perpendicular to the field. (*Right*) Degeneracy can be broken by continuous rotation around an axis perpendicular to the field, resulting in uniaxial alignment of the normal of each nanosheet along the rotation axis. (*C*) Schematic illustration of the film fabrication procedure. A magnetic field is applied to control the orientation of dispersed GO nanosheets, with the orientation preserved by photo-cross-linking the dispersing agents (i.e., monomer: HEMA; cross-linker: ethylene glycol dimethacrylate). GO nanosheets on the surface are exposed by etching away the outer cross-linked polymer (i.e., poly-HEMA) using UV/O_3 oxidation. (*D*) Thickness profile of GO nanosheets obtained by AFM. GO nanosheets had an average sheet height of ∼0.8 nm. (*E*) Polymerization reaction of HEMA to form poly-HEMA under UV irradiation. The poly-HEMA chains are highly cross-linked to form tough and mechanically coherent films, which are resistant to water swelling. (*F*) Photographs of GO composite films with GO nanosheets of different orientations. All of the film samples are 1.6 cm in diameter and 300 μm in thickness. No GO denotes the absence of GO in the polymer film. Random, Vertical, and Planar indicate the orientation of GO nanosheets with respect to the surface of the GO composite film.

Results and Discussion

Composite Films with Aligned GO Nanosheets. To investigate the orientation-dependent interaction of GO with bacteria (Fig. 1*A*), we leverage the magnetic anisotropy of GO to control the orientation of nanosheets by a magnetic field (Fig. 1*B*). In particular, GO nanosheet planes tend to align in parallel to a magnetic field due to the abundant aromatic rings in the sheet plane (26), which gives rise to a random (degenerate) distribution of the normal of the GO nanosheets in the plane perpendicular to the field (Fig. 1*B*, *Left*). Applying the magnetic field perpendicular to the encasing glass substrates enables fabrication of polymer films with vertically aligned GO nanosheets (denoted as "Vertical"; *SI Appendix*, Fig. S1). Additionally, the degeneracy of the GO nanosheets can be broken by continuous rotation around an axis perpendicular to the field, resulting in the uniform alignment of the nanosheet normal axes along the rotation axis (27, 28) (Fig. 1*B*, *Right*). This method enables the fabrication of surfaces with horizontally aligned GO nanosheets (denoted as "Planar"; *SI Appendix*, Fig. S1) by applying the field tangentially through the film, and rotating the glass substrate around the substrate normal. For comparison, GO composite films without alignment (denoted as "Random"; *SI Appendix*, Fig. S1) were also fabricated.

A schematic illustrating the fabrication procedure of the GO composite films is shown in Fig. 1*C*. Suspensions of GO nanosheets (with a thickness of ~0.8 nm; Fig. 1*D*) in 2-hydroxyethyl methacrylate (HEMA), doped with cross-linker and photoinitiator (*SI Appendix*, Fig. S2), were sealed between two glass substrates with a 300-μm spacer and aligned in a magnetic field (6 T). Samples were subsequently cross-linked under UV irradiation to form polymer films, which preserved the orientation of the aligned GO nanosheets (Fig. 1*E*, *Upper*). The composite films were then detached from the glass substrates and irradiated using UV/O_3 to etch away the outer polymer and expose GO nanosheets on the surface. Polymer films without GO (denoted as "No GO") are composed of transparent poly-HEMA polymer, whereas the GO composite films exhibited a dark brown color (Fig. 1*F*) due to the presence of GO nanosheets. The films were tough and mechanically coherent (*SI Appendix*, Fig. S3) and resistant to water swelling, consistent with a high poly-HEMA cross-linking density with the presence of the cross-linker (Fig. 1*E*, *Lower*). This characteristic is critical in preserving the GO orientation in aqueous environments since poly-HEMA is water-soluble and, when cross-linked at low levels, able to swell substantially and form hydrogels. In addition, the cross-linked polymer prevents GO from aggregating or physically rearranging, allowing GO to remain in this state throughout usage of the film. This is highly advantageous in studying the orientation-dependent cytotoxic properties of GO nanosheets.

Field-Strength–Dependent Alignment of GO Nanosheets Suspended in Monomer Solution. The alignment quality of GO nanosheets suspended in the monomer solution at different field strengths was investigated by 2D small-angle X-ray scattering (SAXS). Fig. 2*A* shows 2D SAXS patterns, as well as the azimuthal SAXS intensity, at different field strengths. At a relatively low field strength of 1 T, an elliptical diffusive pattern can be seen in the 2D SAXS pattern. With an increase in field strength to 6 T, the eccentricity of the elliptical shape in the SAXS patterns increases (Fig. 2*A*, *Left*), qualitatively showing a higher degree of GO alignment in a stronger field. This effect can also be clearly seen in the narrowing of the peaks of the azimuthal intensity upon increasing the field strength (Fig. 2*A*, *Right*). The degree of alignment of the GO nanosheets was quantified by correlating the azimuthal dependence of the scattered intensity, $I(\theta)$, to an orientational distribution coefficient, S, by Hermans' distribution function (29). A perfect orientation corresponds to $S = 1$, whereas a completely random orientation possesses an $S = 0$.

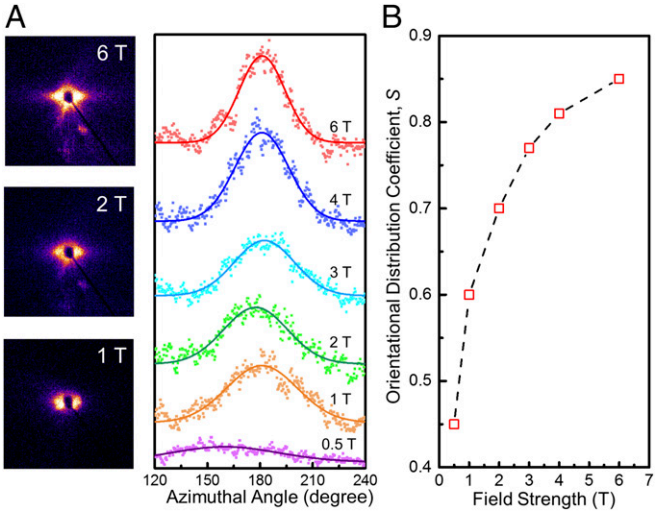

Fig. 2. Alignability of GO nanosheets under different magnetic field strengths in monomer mixture. (*A*) Two-dimensional SAXS patterns and azimuthal dependence of scattering intensity for different field strengths. (*B*) Orientational distribution coefficient, *S*, as a function of field strength. The red squares represent the calculated values of *S* and the dashed line is an eye guide showing the trend of increasing *S* with the increase of field strength. The data were measured by a 2D detector with an accessible range of scattering vector, *q*, of 0.015–0.21 A^{-1} and fitted using Gaussian functions.

Using a Gaussian approximation for $I(\theta)$ within the accessible range of scattering vector q of 0.015–0.21 A^{-1}, we can correlate the full-width at half maximum to S. The orientational distribution coefficient increased with field strength from an $S_{0.5T}$ of 0.45 to an S_{6T} of 0.85 (Fig. 2*B*).

Characteristics of Aligned-GO/Polymer Composite Films. We used the strongest accessible field strength of 6 T to fabricate polymer composites with aligned and exposed GO nanosheets. To confirm preservation of GO orientation after polymerization and cross-linking, we first applied polarized optical microscopy (POM) with crossed polarizers to evaluate the efficacy of rotation in the magnetic field to yield uniform alignment of the GO nanosheets in the composite films (28, 30). As expected, the transmission intensity (I) as determined by $I \propto sin^2 2\varphi$, where φ is the angle between the optical axis (i.e., the normal of GO) and one of the crossed polarizers, reaches its maximum when $\varphi = 45°$ or 135° and its minimum when $\varphi = 0°$ or 90° (*SI Appendix*, Fig. S4). Additionally, transmission intensity in POM images of different GO composite films followed the order Vertical > Random > Planar, indicating that the Vertical-GO film possessed more vertically aligned GO nanosheets within the bulk film compared with the random and planar samples (*SI Appendix*, Fig. S5).

The alignment and orientation of GO nanosheets in the composite films were further confirmed by 2D SAXS analysis. The X-ray beam was propagated through the film plane as illustrated by the schematics of Fig. 3 (*Upper*); the 2D SAXS patterns of the films are exhibited in Fig. 3 (*Middle*). The pure polymer sample did not possess any GO nanosheets, and thus showed negligible scattering intensity. In contrast, the presence of GO nanosheets in the Random-GO film resulted in a substantial rise of scattering intensity, forming a broad and isotropic halo in the 2D SAXS pattern. With magnetic alignment, the Vertical-GO and the Planar-GO films exhibited anisotropic equatorial and meridional scattering patterns, respectively (22), with identical orientational distribution coefficients of ~0.85 (*SI Appendix*, Fig. S6), which unambiguously verified the corresponding orientations of the GO nanosheets in those films.

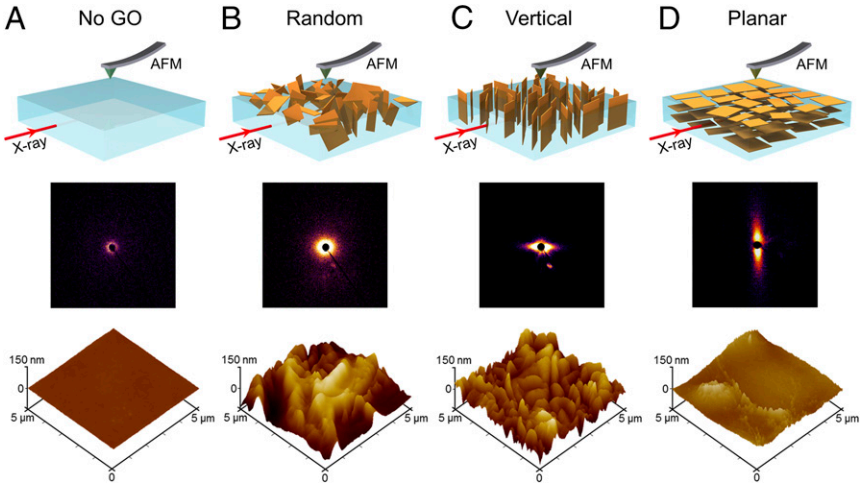

Fig. 3. SAXS and AFM characterizations to determine the GO orientation in bulk and on the surface of GO composite films, respectively. The X-ray beam is positioned parallel to the film plane, and the AFM probe scans the surface, as illustrated in the corresponding 3D cartoons. (*A*) Polymer film possessing no GO nanosheets shows negligible scattering intensity in SAXS, and has a smooth surface as revealed by AFM height image. (*B*) Random orientation of GO nanosheets without magnetic alignment gives rise to a broad, isotropic halo in the 2D SAXS pattern. The AFM image reveals a sharp increase in roughness, indicating the presence of partially exposed GO nanosheets. (*C*) Anisotropic equatorial scattering shown in the 2D SAXS pattern indicates the vertical alignment of the GO nanosheets in the polymer film. AFM results demonstrate that the vertically aligned nanosheets are partially exposed. (*D*) Anisotropic meridional scattering shown in the 2D SAXS pattern confirms the in-plane alignment of the GO nanosheets in the polymer film. The AFM image shows a smoother surface with the GO nanosheets aligned nearly parallel to the surface plane.

The surface morphology of the films was characterized using atomic force microscopy (AFM). AFM results (Fig. 3, *Lower* and *SI Appendix*, Fig. S7) confirmed that the UV/O_3 etching exposed GO nanosheets on the surface, and that the alignment of GO nanosheets for surface-exposed GO was the same as for GO within the bulk film. In particular, the surface of the Random-GO film was composed of sloped ridges and deep valleys, the Vertical-GO film had visibly sharp ridges, and the Planar-GO film showed a much smoother surface, as expected for exposed, near-horizontal GO nanosheets. Unetched films did not show the presence of GO edges on their respective surfaces (*SI Appendix*, Figs. S8 and S9), as the GO nanosheets were likely covered by a layer of polymer (*SI Appendix*, Fig. S10).

Enhanced Antibacterial Activity of Vertically Aligned GO Nanosheets. The antibacterial activity of the GO composite films was evaluated using a live/dead fluorescent staining assay (31–33). Briefly, films were contacted with *E. coli*, a model gram-negative bacteria, in suspension for 3 h, after which surface-attached bacteria were stained with SYTO 9 dye and propidium iodide for live and dead cells, respectively. The ratio of live bacteria against the total number of bacteria (both live and dead) was calculated to determine the antibacterial activity of the films. Bacterial inactivation was found to be affected by the orientation of the GO nanosheets (Fig. 4*A*). In particular, the Vertical-GO film showed lower cell viability (56.0 ± 8.7%) than the Random-GO film (75.3 ± 3.5%) and the Planar-GO film (81.8 ± 5.1%), suggesting that antibacterial activity is enhanced for films with vertically aligned GO nanosheets.

To further probe their relative cytotoxicity, GO films were contacted with *E. coli* and colony-forming units (cfu) of bacteria attached to the surface were enumerated. Briefly, after the bacteria exposure, attached live cells on the films were detached from the surface by mild sonication in saline solution, and subsequently cultured on solid media and incubated overnight (13, 32, 34). Note that for these experiments, cfu data are influenced not only by cytotoxicity but also by the ability of bacteria to adhere to the surface. For this reason, only the films containing GO nanosheets were used to have similar material properties for bacterial adhesion. The cfu data were normalized to the data of the Random-GO film for comparison (Fig. 4*B*). A similar relationship between GO orientation and antibacterial activity was observed, namely, the Vertical-GO film showed lower viability of *E. coli* cells compared with the Random-GO film and the Planar-GO film, again demonstrating enhanced bacterial inactivation for films with vertically aligned GO nanosheets.

After the exposure to the GO composite films, morphological changes of the attached cells were observed using scanning electron microscopy (SEM; Fig. 4 *C*–*F* and more images in *SI Appendix*, Fig. S11). Due to the biocompatibility of poly-HEMA (35), the bacteria on the No-GO film showed intact cell morphology. Among the GO composite films, the cells on the Random-GO and Planar-GO films retained their morphological integrity, whereas the cells on the Vertical-GO films became flattened and wrinkled, suggesting loss of viability and possible damage to the cell membrane.

Taken together, the results from the live/dead assay, plate-counting assay, and morphology observations indicate that the vertically aligned GO nanosheets had stronger antibacterial activity than the nonaligned (i.e., random) or horizontally aligned (i.e., planar) samples. We surmised that this orientation-dependent cell inactivation could be related to the density of exposed GO edges with preferential orientation for bacteria inactivation. However, conflicting conclusions exist in the literature on the mechanisms of GO interaction with living cells (36), complicating the interpretation of our results. Further mechanistic investigations were needed to elucidate the exact contribution of alignment (i.e., exposure of edges) on the orientation-dependent antibacterial activity of GO nanosheets.

Proposed Mechanism for the Enhanced Antibacterial Activity of Vertically Aligned GO Nanosheets. Several antibacterial mechanisms have been postulated for GO, which can be classified into two main categories: physical disruption and chemical oxidation (37, 38). To determine what mechanisms are responsible for the enhanced antibacterial activity of the vertically aligned GO nanosheets, we used lipid vesicles and chemical probes to determine the contributions of physical and chemical mechanisms, respectively. Note that due to the small amount of exposed GO on the surface of the films, the exploration of mechanisms required the use of free GO nanosheets suspended in solution, which also possessed antibacterial activity as evidenced by cfu enumeration assay (*SI Appendix*, Fig. S12), similar to the results of previous studies (4, 11).

Physical Disruption of Lipid Bilayer Membrane Induced by GO Nanosheets. The exact role of physical membrane disruption in the overall cytotoxic effects of GO is still unclear. Although simulations have provided some mechanistic insight into the physical interactions between GO and biological membranes (7, 39), these modeling studies have also yielded conflicting conclusions, such as whether or not the piercing of cell membranes compromises membrane integrity (7, 9), demonstrating the need

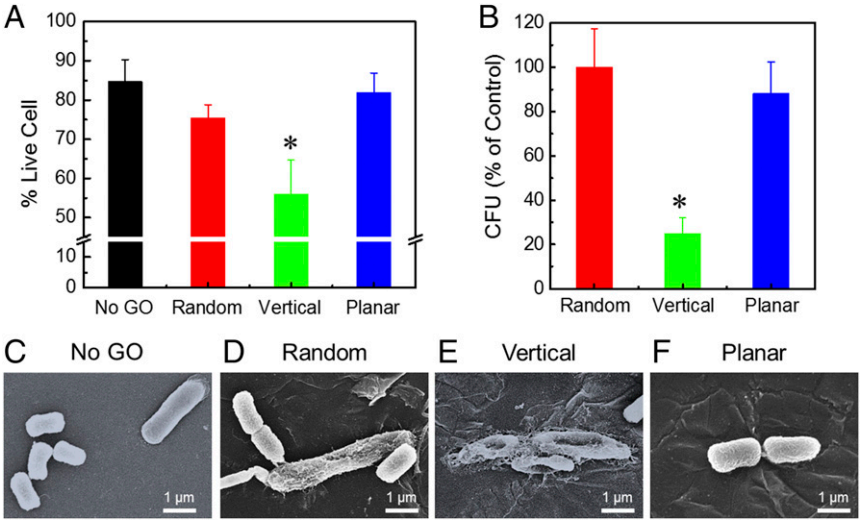

Fig. 4. Antibacterial activity of GO composite films with different orientations of GO nanosheets. (*A*) Cell viability of deposited *E. coli* cells after 3 h of contact with surfaces with aligned GO nanosheets, determined by live/dead fluorescent staining assay. Values marked with an asterisk (*) are significantly different from the value of No-GO sample ($n = 3$; Student's *t* test, $P < 0.05$). (*B*) Relative number of viable *E. coli* cells after 3 h of contact with surfaces with aligned GO, determined by cfu plate counting and normalized to the results of the Random-GO surface. The No-GO surface was not used as a control due to decreased bacterial adhesion stemming from the smooth and hydrophilic nature of the poly-HEMA surface. Values marked with an asterisk (*) are significantly different from the value of Random sample ($n = 3$; Student's *t* test, $P < 0.05$). Representative SEM micrographs of *E. coli* cells on polymer films with No GO (*C*) and Random (*D*), Vertical (*E*), and Planar (*F*) GO nanosheets. The bacteria on the No-GO film showed intact cell morphology. Among the GO composite films, the cells on the Random-GO and Planar-GO films largely retained their morphological integrity, whereas the cells on the Vertical-GO films became flattened and wrinkled, suggesting loss of viability and possible damage to the cell membrane.

for proper experimental validation. However, to date, experimental evidence of physical disruption has been largely qualitative and anecdotal, primarily based on microscopy images that show the uptake of nanosheets by cells (36, 37). A conclusive and quantitative demonstration of physical membrane disruption by GO is lacking.

We utilized phospholipid vesicles to mimic GO–cell interactions. While lipid vesicles are an imperfect model for bacteria and other living cells due to the complexity of true cell membranes, the simplified membranes of lipid vesicles allow for mechanistic elucidation (40). In our study, suspensions of monodisperse, 140-nm-diameter, unilamellar vesicles were produced with a high concentration (50 mM) of encapsulated fluorescent dye [5(6)-carboxyfluorescein] and no dye initially present in the extravesicular solution. At this concentration, self-quenching of the highly concentrated dye results in negligible fluorescence intensity in the pristine vesicle suspension (41). Leakage of the fluorophore into the extravesicular solution eliminates the self-quenching behavior, resulting in an increase in total fluorescence intensity that can be linearly related to the volume of the leaked solution. Therefore, when contacted with the GO nanosheets, this system allows for quantitative measurement of the loss of membrane integrity due to damage to the lipid bilayer.

Fig. 5*A* presents the fluorophore concentration in the extravesicular solution vs. contact time. The blank solution did not show any increase of extravesicular fluorophore concentration, indicating that the lipid bilayer is impermeable on the relevant time scale to the charged fluorescent dye. In contrast, lipid vesicle suspensions that were contacted with GO nanosheets showed substantial increases in extravesicular fluorophore concentration, which readily reach an equilibrium of 70% of total fluorophore concentration after 1 h of contact, indicating that the presence of GO nanosheets induces a remarkably rapid rate in loss of vesicle integrity.

Although the loss of vesicle integrity observed here is indicative of physical membrane disruption as predicted by previous modeling (9, 10), it may be possible for chemical oxidation to degrade phospholipids and similarly induce membrane defects (42). To evaluate this possibility, lipid vesicles were exposed to solutions with different oxidative conditions involving relatively high concentrations of two different types of ROS: hydrogen peroxide (H_2O_2) and hydroxyl radicals (generated through UV-irradiated activation of H_2O_2). H_2O_2 is a mild oxidant with a redox potential of 1.76 V (43), which was used as a positive control in previous studies that quantified the amount of oxidation induced by GO (11, 12, 32, 44). Hydroxyl radicals are even more reactive, with a redox potential of 2.7 V (45).

The exposure of lipid vesicles to each oxidant (H_2O_2 and hydroxyl radicals) did not result in an increase in extravesicular fluorophore concentration (squares in Fig. 5*A*), which differed from the substantial leakage of fluorophore when vesicles were exposed to the GO nanosheets. For each time point, we added a nonionic surfactant to solubilize the lipid vesicles and release all entrapped fluorophore to determine the total fluorophore concentration (circles in Fig. 5*A*). The total fluorophore concentration remained stable when exposed to H_2O_2 and decreased by $31 \pm 1\%$ when exposed to hydroxyl radical. The lower fluorophore concentration upon hydroxyl radical exposure is likely caused by hydroxyl radical-mediated degradation inside the vesicles. However, even under such intense oxidative conditions, we still did not observe leakage of the fluorescent dye. Taken together, these results strongly indicate that the loss of membrane integrity in the GO/lipid vesicle system is solely caused by physical disruption of the bilayer structure induced by GO nanosheets, as schematically illustrated in Fig. 5*B*.

Electron-Transfer Oxidation of Intracellular Compounds Mediated by GO Nanosheets. Oxidative stress mediated by GO is another major mechanism for its antibacterial activity. Higher exposure of edges on the Vertical-GO film may result in higher exposure of defects, thus providing more active sites for mediating oxidative stress (12, 32). Nevertheless, conflicting conclusions exist for the mechanism of chemical oxidation, in particular, whether GO-mediated oxidative stress is induced indirectly via ROS generation (36, 46, 47) or directly via electron-transfer pathway (11). While direct contact

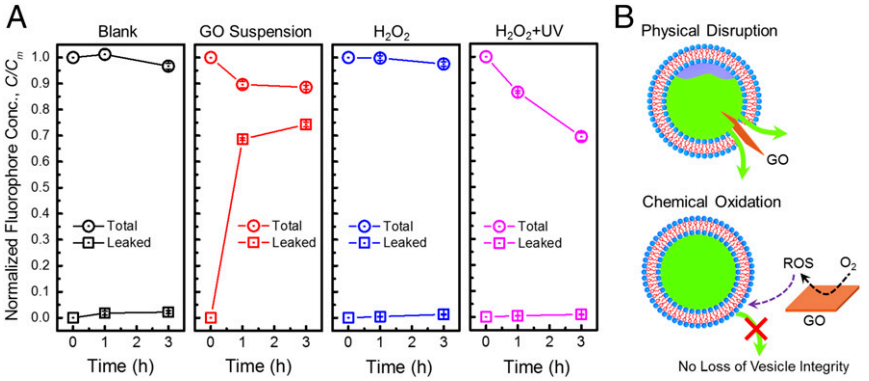

Fig. 5. Physical disruption of phospholipid vesicles by GO nanosheets. (*A*) Comparison of leaked (squares) and total (circles) concentrations (Conc.) of fluorescent dye in blank solution, and exposed to GO suspension (40 μg·mL^{-1}), 30 mM H_2O_2, and hydroxyl radicals generated using 30 mM H_2O_2 with UV irradiation (254 nm). For the leaked fluorophore values, the fluorescence of the solution was directly measured. For the total fluorophore values, the nonionic surfactant Triton X-100 was added to 0.5 wt/vol%, solubilizing the lipid vesicles and releasing all entrapped fluorophore, after which the fluorescence was measured again. The solutions contained lipid vesicles at 0.1 mg·mL^{-1} with a high concentration (50 mM) of internal carboxyfluorescein dye. Total fluorescence increased upon dye leakage due to relief of fluorescence self-quenching. C/C_m, normalized fluorophore concentration. (*B*) Schematic illustrating different mechanisms of interaction between GO nanosheets and vesicles. The substantial leakage of fluorophore with the presence of GO, together with the negligible effect of oxidative conditions, suggests that physical disruption (*Upper*) induced by GO nanosheets was the major cause for the loss of vesicle integrity rather than chemical oxidation (*Lower*).

of nanosheets and cell membranes is not necessary for ROS-mediated oxidation, electron-transfer oxidation requires more intimate contact (e.g., insertion of GO into the cell membrane) to achieve bacterial inactivation (11, 31, 36, 48). Herein, we utilized chemical probes to investigate the relative importance of direct electron-transfer oxidation and indirect ROS-mediated oxidation.

We first selected a model intracellular compound, glutathione (12, 32, 44), to evaluate the oxidative stress of GO. Glutathione is a thiol-containing peptide that is present in most gram-negative bacteria (49) as an endogenous antioxidant to prevent damage to cellular components caused by oxidative stress (50, 51). This compound has been widely used as an oxidative stress indicator (12, 51, 52). Glutathione was exposed to 200 μg·mL^{-1} GO nanosheets for 3 h (Fig. 6*A*, *Left*), which were under the same aerobic condition (8.7 mg·L^{-1} dissolved oxygen, *SI Appendix*, Fig. S13) as the experiments in the above sections. Compared with the marginal amount of glutathione oxidized in the control sample (3.2%), the amount of glutathione oxidation upon exposure to GO nanosheets (27.6%) was much more pronounced, suggesting the importance of GO in catalyzing the oxidation of glutathione (Fig. 6*F*). We also performed GO exposure experiments under an anoxic condition, in which the solution was purged with nitrogen gas for 30 min before the experiments to remove most of the dissolved oxygen (residual oxygen concentration was 0.4 mg·L^{-1}; *SI Appendix*, Fig. S13). Under the anoxic condition, loss of glutathione with the presence of GO was only 4.9%, which is much lower than that under the aerobic condition (27.6%), indicating that the oxidation of glutathione was substantially inhibited when oxygen is lacking.

While the glutathione results demonstrate that GO can catalyze chemical oxidation, this oxidation could stem from both ROS generation and direct electron transfer. Therefore, we also assessed the generation of the four most important ROS [i.e., singlet oxygen ($^1O_2$), hydroxyl radical ($^{\bullet}OH$), superoxide radical anion ($O_2^{\bullet-}$), and H_2O_2] in a solution of dispersed GO using four different chemical probes. The results show that there was no detectable generation of $^1O_2$, $^{\bullet}OH$, or $O_2^{\bullet-}$ and minor formation (~1.76 μM) of H_2O_2 (Fig. 6 *B*–*E*). Experiments were also performed in the presence of both GO and suspended bacteria. A negligible difference in ROS generation was observed compared with solutions with GO only (*SI Appendix*, Fig. S14). The small amount of H_2O_2 likely accumulated during the long-term storage of GO via marginal reduction of O_2, thus representing a steady concentration in the GO bulk solution phase. Using pure H_2O_2 (without GO) with similar concentration (2 μM), we observed negligible oxidation of glutathione (*SI Appendix*, Fig. S15). Taken together, these results demonstrate that the GO-mediated oxidation of glutathione under aerobic conditions stemmed from electron transfer to oxygen catalyzed by GO (Fig. 6*F*). Additionally, the limited toxicity for *E. coli* (*SI Appendix*, Fig. S16) upon exposure to 2 μM H_2O_2 further indicates that although GO nanosheets could produce trace amounts of free ROS (i.e., H_2O_2), the generation of free ROS is not the major mechanism in oxidative stress-mediated antibacterial activity of GO nanosheets. We therefore conclude that the direct pathway (i.e., electron-transfer oxidation) is the major chemical cause for the cytotoxicity of GO nanosheets.

Combined Effect of Physical and Chemical Mechanisms for Edge-Mediated Antibacterial Activity. The experiments with dispersed GO offer mechanistic insight into the enhanced antibacterial activity of the Vertical-GO film. First, considering the ability of GO to disrupt lipid bilayers, it is likely that GO nanosheets could also penetrate the cell membrane and directly inactivate the bacterial cell. While pure lipid bilayers are an imperfect model of complex cell membranes, they do share many physicochemical properties (40, 53). As shown by POM, SAXS, and AFM characterization, compared with the Random-GO and Planar-GO films, the Vertical-GO films contained more exposed edges with a vertical orientation. Vertically oriented nanosheets are more likely to interact with bacteria in an orthogonal fashion, which was shown by modeling studies to be energetically favorable for penetration of the lipid bilayer (7, 8). The enhanced cytotoxicity of the Vertical-GO film matches this expectation for increased orientation-dependent physical membrane disruption.

Second, the degradation of the model intracellular compound (glutathione) suggests that GO nanosheets could mediate substantial oxidative stress on the cell, which would also contribute to the cytotoxicity of GO. However, due to the lack of sufficient generation of free ROS to oxidize the cellular compounds, the oxidative stress-induced antibacterial activity would mainly rely on the electron-transfer oxidation pathway, in which direct contact of GO nanosheets with intracellular compounds is needed to exert its effect (11, 31). Due to the enhanced physical penetration induced by the exposed edges on the Vertical-GO film, greater levels of electron transfer would occur, during

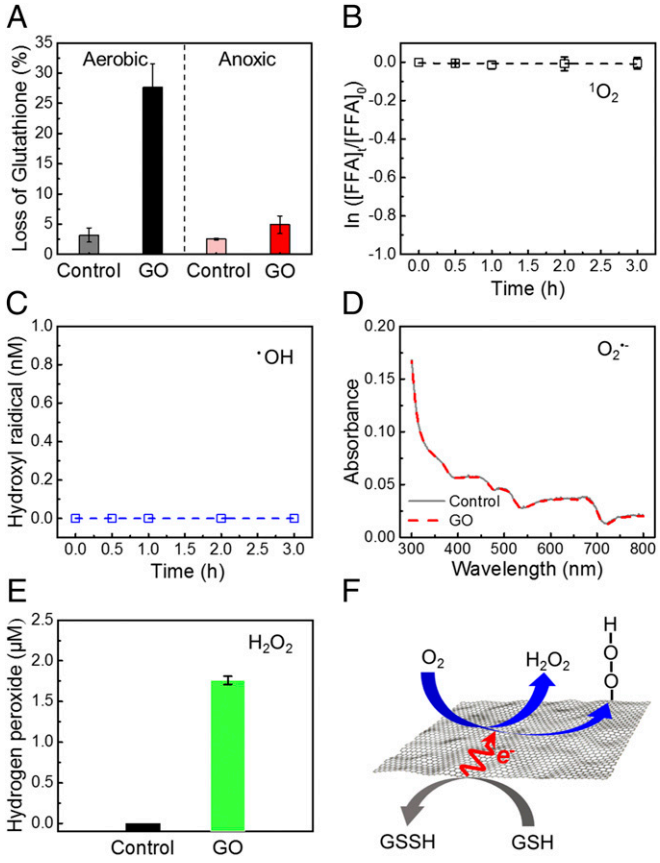

Fig. 6. Major role of electron-transfer oxidation in chemical toxicity of GO nanosheets. (*A*) In vitro glutathione oxidation by GO nanosheets in suspension. Glutathione (0.4 mM) was exposed to 0 (control) or 200 μg·mL^{-1} GO in bicarbonate buffer (50 mM, pH 8.6) at room temperature for 3 h. (*Left*) For the aerobic condition, the solution was prepared without any treatment and the dissolved oxygen was ~8.7 mg·L^{-1}. (*Right*) For the anoxic condition, the solution was purged with nitrogen gas for 30 min to decrease the dissolved oxygen to ~0.4 mg·L^{-1}. (*B–E*) ROS generation in the 200 μg·mL^{-1} GO solution detected with ROS probes. The experiments were conducted in the dark for 3 h at room temperature. (*B*) Generation of $^1O_2$ is indicated by decay of furfuryl alcohol (FFA; initial concentration of 50 μM). (*C*) Cumulative •OH generation over time is indicated by the formation of hydroxyterephthalate. (*D*) Generation of $O_2^{\bullet-}$ indicated by the reduction of 2,3-Bis-(2-methoxy-4-nitro-5-sulfophenyl)-2H-tetrazolium-5-carboxanilide (initial concentration of 100 μM). (*E*) H_2O_2 concentration measured by the Amplex Red assay. (*F*) Schematic illustrating electron-transfer oxidation of a model intracellular compound, glutathione (GSH), mediated by a GO nanosheet. Each glutathione molecule donates one electron to form its corresponding oxidized dimer, glutathione disulfide (GSSH). The GO nanosheet works as an electron shuttle to transfer electrons to dissolved oxygen, which subsequently forms H_2O_2 or surface-bound peroxide intermediates at edge or defect sites of GO nanosheets.

which GO serves as a conductive bridge over the insulating lipid bilayer to release cellular energy [electron donor (e.g., glutathione)] into the external environment [electron acceptor (e.g., oxygen)] (11, 44), thereby degrading intracellular compounds to cause cell death. It must be noted that the chemical and physical mechanisms described here both require direct, edge-mediated contact with cells. It is likely that both mechanisms contributed to the enhanced antibacterial activity of the Vertical-GO film.

Materials and Methods

Fabrication of Composite Films with Aligned and Exposed GO Nanosheets. HEMA (monomer, 97%; Sigma–Aldrich) was mixed with ethylene glycol dimethacrylate (EGDMA; cross-linker, 98%; Sigma–Aldrich) and 4,4′-Azobis(4-cyanovaleric acid) (ACVA; photoinitiator, 98%; Sigma–Aldrich) to form a HEMA mixture (HEMA/EGDMA/ACVA = 100:10:0.5 by weight). To form GO/HEMA mixtures, an aqueous GO suspension (6.2 g·L^{-1}; Graphene Supermarket) was washed twice using the HEMA mixture and suspended at a final concentration of 2.1 g·L^{-1}.

To fabricate GO/polymer composite films, an aliquot of the GO/HEMA mixture solution was sealed between two glass slides with a thickness of 300 μm and subsequently placed in a superconducting magnet (American Magnetics, Inc.) at a field strength of 6 T for 30 min at 20 °C to align the GO nanosheets. The sample was then immediately photo-cross-linked by exposure to 365 nm of UV light at room temperature to form a solid composite film. After removing the glass slides, the film was irradiated in a UV/O_3 chamber (MTI Corporation) for 2 h to etch away the top polymer layer and produce a surface with exposed GO nanosheets. The films were stored in deionized water overnight to remove residual unreacted chemicals.

Characterization of Alignment and Exposure of GO Nanosheets. The alignment of GO nanosheets was evaluated using POM and SAXS. Additionally, the surface morphology of the films was characterized using AFM and SEM. POM studies were performed using an Axiovert 200 M inverted microscope (Zeiss). SAXS was performed using a Rigaku SMAX-3000 instrument with the accessible scattering vector (q) ranging from 0.015 to 0.21 Å^{-1}. The propagation of the X-ray beam was orthogonal to the normal of the exposed surface (Fig. 3). The method to quantify the alignment degree (i.e., orientational distribution coefficient, S) of GO nanosheets is provided in the *SI Appendix*. Film surface morphology was characterized using a Dimension FastScan AFM system (Bruker). Imaging of the samples was performed in peak force tapping mode with silicon probes (Scanasyst-Air; Bruker). The probe had a spring constant of 0.4 N·m^{-1}, resonance frequency of 70 kHz, and cantilever length of 115 ± 15 μm. Film surface morphology was also observed through a field emission scanning electron microscope (SU-70; Hitachi) with an accelerating voltage of 5 kV. Film samples were air-dried overnight before the measurements and sputter-coated with an 8-nm-thick layer of iridium.

Antibacterial Activity of the GO Nanosheets. *E. coli* (American Type Culture Collection BW26437) was received from the Yale *E. coli* Genetic Stock Center. Bacteria were grown overnight in Luria-Bertani (LB) broth at 37 °C. After incubation, the cultures were diluted in fresh medium and grown until log phase (~2 h), which was defined as reaching an optical density of 0.8 at 600 nm. The bacterial cells were washed three times with sterile saline solution (0.9% NaCl) before use.

Cell viability was determined using a live/dead fluorescent staining assay, as reported in previous studies (31–33). Briefly, the bacterial suspension (10^8 cfu·mL^{-1}) was exposed to films for 3 h at room temperature. After discarding the excess bacterial suspension, 5-mL saline solution was used to rinse unattached cells from the film. The film was then transferred to 10-mL saline solution and sonicated for 10 min in an ultrasonic bath (26 W·L^{-1}, FS60 Ultrasonic Cleaner) to detach bacteria from the film surface. Then, 1.17 μM SYTO 9 and 10 μM propidium iodide (Live/Dead Baclight Bacterial Viability Kit; Thermo Fisher) were added into the supernatant to stain live and dead cells, respectively. After 15 min of staining, the supernatant was filtered through a membrane (0.2 μm polytetrafluoroethylene; EMD Millipore) to deposit the stained cells. The membrane was then transferred to a microscopic slide and visualized using an epifluorescence microscope (Axiovert 200 M; Zeiss). For each sample, fluorescent images were captured and cells were enumerated for five random locations, with each location containing at least 200 cells (including both live and dead cells). Three independent samples were assessed for each orientation, and viability was calculated from the numbers of the live (green) and dead (red) cells.

A cfu enumeration assay was used to evaluate the antibacterial activity of GO composite films, following the protocol developed in previous studies (13, 32, 34). Cells were exposed to films as described for the live/dead assay. After cell removal from the film surface via bath sonication, the supernatant was immediately cultured on LB agar media and incubated overnight at 37 °C for cfu enumeration. For each orientation, three independent samples were exposed to *E. coli* and the average value with one standard derivation was reported. The normalized cfu for each sample was calculated in reference to the cfu of the sample with nonaligned GO.

To evaluate the toxicity of GO in suspension, *E. coli* suspension (10^7 cfu·mL^{-1}) was exposed to GO nanosheets (200 μg·mL^{-1}) for 3 h at room temperature under constant agitation. At the end of the exposure period, the bacterial suspension was bath-sonicated (26 W·L^{-1}, FS60 Ultrasonic Cleaner) for 10 min to break aggregates, which might cause discrepancies in the cfu analysis (32, 54). Then, bacterial suspensions were immediately cultured on LB agar media and incubated overnight at 37 °C for cfu enumeration.

Cell morphologies of bacteria deposited on films were visualized by SEM as previously described (14, 32, 34). After exposure to bacteria cells for 3 h, films were gently washed with saline solution and fixed with Karnovsky's fixative

[2% paraformaldehyde, 2.5% glutaraldehyde in 0.2 M Sorenson's buffer (pH 7.2)] for 3 h. Samples were then dehydrated by a sequential immersion in water/ethanol (50:50, 30:70, 20:80, 10:90, and 0:100) and ethanol/freon (50:50, 25:75, and 0:100), and left to dry overnight in a desiccator at room temperature. Samples were sputter-coated with 8 nm of iridium and imaged by SEM.

Physical Contact of Liposomes with Exposed GO Nanosheets. Dye-leakage experiments were performed by exposing liposomes encapsulating a fluorescent dye solution [50 mM 3-(*N*-morpholino)propanesulfonic acid (MOPS), 50 mM 5(6)carboxyfluorescein (pH 7.5)] to a GO suspension. Monodisperse liposome stock solutions were prepared using 1,2-dioleoyl-sn-glycero-3-phosphocholine (DOPC; Avanti Polar Lipids) via the film rehydration and extrusion methods (*SI Appendix*), buffer-exchanged, and subsequently diluted with 50 mM MOPS and 90 mM NaCl (pH 7.5) to obtain a final DOPC concentration of 0.1 mg·mL^{-1}. The vesicle solution exhibited a low background fluorescence intensity as the encapsulated fluorescent dye self-quenches at high concentration (above 10 mM). An aliquot of the liposome solution (20 mL) was added to a glass vial containing 40 μg·mL^{-1} GO suspension to initiate exposure. Dye leakage into the extravesicular solution eliminated self-quenching and led to a linear increase in fluorescence. After exposure, samples were taken and centrifuged at 13,000 rpm (Micro 1818; VWR) to remove potential GO/liposome aggregates. Fluorescence of the supernatant was measured using a spectrofluorometer (Synergy HT; BioTek Instruments) at excitation and emission wavelengths of 485 nm and 528 nm, respectively. After measuring the leaked fluorescence intensity, the nonionic surfactant Triton X-100 (Fisher) was added to a concentration of 0.5 wt/vol%, solubilizing the lipid vesicles and releasing all entrapped fluorophore. The fluorescence was then measured again and denoted as total fluorescence intensity. In the concentration range of interest (0–10 μM), the fluorophore concentration is linearly related to the fluorescence intensity (*SI Appendix*, Fig. S17). Additionally, GO has negligible adsorption of fluorophore in vesicle suspension (*SI Appendix*, Fig. S18). Therefore, the normalized fraction of the leaked fluorophore, C/C_m, which quantitatively indicates the loss of membrane integrity due to damage to the lipid bilayer, can be calculated from

$$\frac{C}{C_m}=\frac{I_t-I_0}{I_m-I_0}, \quad [1]$$

where C_m is the maximum concentration of dye upon liposome solubilization, I_t is the measured fluorescence intensity, I_0 is the initial intensity before exposure to GO, and I_m is the fluorescence intensity upon liposome solubilization.

To evaluate the effect of oxidation on liposome integrity, dye-encapsulated liposomes were exposed to solutions with two types of oxidants: H_2O_2 and hydroxyl radicals (generated through UV-irradiated activation of H_2O_2). Briefly, 30 mM H_2O_2 was added into glass vials containing 0.1 mg·mL^{-1} liposome solution, which were either stored in the dark or exposed to 254 nm of UV light. The procedure to quantify leaked fluorophore was identical to that used for the GO suspension sample.

Glutathione Oxidation Assay. Glutathione oxidation mediated by GO was measured in acellular conditions using a procedure adapted from previous publications (11, 32, 44). GO suspension (200 μg·mL^{-1}) was added into a glass vial containing 0.4 mM glutathione (Sigma–Aldrich) dissolved in 50 mM bicarbonate buffer (pH 8.6) to initiate the reaction, during which the glass vials were in the dark and agitated for 3 h at room temperature. The amount of unoxidized glutathione was quantified spectrophotometrically (412 nm) using Ellman's reagent [5,5′-dithiobis(2-nitrobenzoic acid) (DTNB); Acros Organics]. Specifically, GO nanosheets were filtered out of the solution (0.22 μm polyethersulfone; Millimex). Then, 450 μL of the filtered solution was added to 780 μL of Tris·HCl buffer (pH 8.3), followed by addition of 20 μL of 100 mM DTNB stock solution. The percent loss of glutathione is calculated in reference to the absorbance measurements of a control sample without GO.

The glutathione reaction was performed under aerobic and anoxic conditions. For aerobic conditions, the solution was prepared without any treatment, resulting in a dissolved oxygen concentration of ∼8.7 mg·L^{-1}. To create anoxic conditions, the solution was purged with nitrogen gas for 30 min, decreasing the dissolved oxygen to ∼0.4 mg·L^{-1} (*SI Appendix*, Fig. S13*A*). The reaction vials were tightly sealed with rubber caps, and the dissolved oxygen was near constant for both aerobic and anoxic conditions over the course of the 3-h reaction (*SI Appendix*, Fig. S13*B*).

Measurement of ROS in GO Suspension. The generation of the four most important ROS (i.e., $^1O_2$, $^{\bullet}OH$, $O_2^{\bullet-}$, and H_2O_2) was assessed in a solution of dispersed GO using respective chemical probes. Solutions containing 200 μg·mL^{-1} GO and individual ROS probe were stored in the dark at room temperature. Aliquots of the solution were taken at various time points for kinetic analysis of ROS generation. Additionally, formation of ROS induced by GO was measured in bacterial suspensions (10^7 cfu·mL^{-1} *E. coli*). Details of ROS measurement methodologies are provided in the *SI Appendix*.

ACKNOWLEDGMENTS. We acknowledge the support received from the US National Science Foundation (NSF) under Award CBET-1437630 and through the NSF Nanosystems Engineering Research Center for Nanotechnology-Enabled Water Treatment (Grant EEC-1449500). We also acknowledge the NSF Graduate Research Fellowship (DGE-1122492) awarded to J.R.W., the Early Postdoctoral Mobility Fellowship awarded by Swiss National Science Foundation (P2EZP2_168796 to C.C.), and the use of facilities supported by the Yale Institute for Nanoscience and Quantum Engineering from NSF under Grant DMR-1119826.

1. Novoselov KS, et al. (2004) Electric field effect in atomically thin carbon films. *Science* 306:666–669.
2. Xu M, Liang T, Shi M, Chen H (2013) Graphene-like two-dimensional materials. *Chem Rev* 113:3766–3798.
3. Geim AK, Novoselov KS (2007) The rise of graphene. *Nat Mater* 6:183–191.
4. Akhavan O, Ghaderi E (2010) Toxicity of graphene and graphene oxide nanowalls against bacteria. *ACS Nano* 4:5731–5736.
5. Liao K-H, Lin Y-S, Macosko CW, Haynes CL (2011) Cytotoxicity of graphene oxide and graphene in human erythrocytes and skin fibroblasts. *ACS Appl Mater Interfaces* 3:2607–2615.
6. He J, et al. (2015) Killing dental pathogens using antibacterial graphene oxide. *ACS Appl Mater Interfaces* 7:5605–5611.
7. Li Y, et al. (2013) Graphene microsheets enter cells through spontaneous membrane penetration at edge asperities and corner sites. *Proc Natl Acad Sci USA* 110: 12295–12300.
8. Wang JL, Wei YJ, Shi XH, Gao HJ (2013) Cellular entry of graphene nanosheets: The role of thickness, oxidation and surface adsorption. *RSC Adv* 3:15776–15782.
9. Pham VTH, et al. (2015) Graphene induces formation of pores that kill spherical and rod-shaped bacteria. *ACS Nano* 9:8458–8467.
10. Tu Y, et al. (2013) Destructive extraction of phospholipids from Escherichia coli membranes by graphene nanosheets. *Nat Nanotechnol* 8:594–601.
11. Liu S, et al. (2011) Antibacterial activity of graphite, graphite oxide, graphene oxide, and reduced graphene oxide: Membrane and oxidative stress. *ACS Nano* 5:6971–6980.
12. Liu X, et al. (2011) Antioxidant deactivation on graphenic nanocarbon surfaces. *Small* 7:2775–2785.
13. Perreault F, Tousley ME, Elimelech M (2013) Thin-film composite polyamide membranes functionalized with biocidal graphene oxide nanosheets. *Environ Sci Technol Lett* 1:71–76.
14. de Faria AF, Perreault F, Shaulsky E, Arias Chavez LH, Elimelech M (2015) Antimicrobial electrospun biopolymer nanofiber mats functionalized with graphene oxide-silver nanocomposites. *ACS Appl Mater Interfaces* 7:12751–12759.
15. Zhao J, et al. (2013) Graphene oxide-based antibacterial cotton fabrics. *Adv Healthc Mater* 2:1259–1266.
16. Hu W, et al. (2010) Graphene-based antibacterial paper. *ACS Nano* 4:4317–4323.
17. Perreault F, et al. (2016) Biofouling mitigation in forward osmosis using graphene oxide functionalized thin-film composite membranes. *Environ Sci Technol* 50: 5840–5848.
18. Bowling RJ, Packard RT, McCreery RL (1989) Activation of highly ordered pyrolytic graphite for heterogeneous electron transfer: Relationship between electrochemical performance and carbon microstructure. *J Am Chem Soc* 111:1217–1223.
19. Qu D (2007) Investigation of oxygen reduction on activated carbon electrodes in alkaline solution. *Carbon* 45:1296–1301.
20. Sharma R, Baik JH, Perera CJ, Strano MS (2010) Anomalously large reactivity of single graphene layers and edges toward electron transfer chemistries. *Nano Lett* 10: 398–405.
21. Kim JY, Kim SO (2014) Liquid crystals: Electric fields line up graphene oxide. *Nat Mater* 13:325–326.
22. Wu L, et al. (2014) Magnetically induced anisotropic orientation of graphene oxide locked by in situ hydrogelation. *ACS Nano* 8:4640–4649.
23. Paredes JI, Villar-Rodil S, Martínez-Alonso A, Tascón JMD (2008) Graphene oxide dispersions in organic solvents. *Langmuir* 24:10560–10564.
24. de Gennes PG, Prost J (1993) *The Physics of Liquid Crystals* (Oxford Univ Press, Clarendon, Oxford), 2nd Ed.
25. Firouzi A, Schaefer DJ, Tolbert SH, Stucky GD, Chmelka BF (1997) Magnetic-field-induced orientational ordering of alkaline lyotropic silicate–surfactant liquid crystals. *J Am Chem Soc* 119:9466–9477.
26. Pauling L (1936) The diamagnetic anisotropy of aromatic molecules. *J Chem Phys* 4:673–677.
27. Emsley JW, Lindon JC, Luckhurst GR, Shaw D (1973) Nuclear magnetic resonance studies of magnetohydrodynamic effects in the nematic mesophase. *Chem Phys Lett* 19:345–347.

28. Feng X, et al. (2014) Scalable fabrication of polymer membranes with vertically aligned 1 nm pores by magnetic field directed self-assembly. *ACS Nano* 8:11977–11986.
29. Hermans JJ, Hermans PH, Vermaas D, Weidinger A (1946) Quantitative evaluation of orientation in cellulose fibres from the X-ray fibre diagram. *Recl Trav Chim Pays Bas* 65:427–447.
30. Dierking I (2003) *Textures of Liquid Crystals* (Wiley, Weinheim, Germany).
31. Kang S, Herzberg M, Rodrigues DF, Elimelech M (2008) Antibacterial effects of carbon nanotubes: Size does matter! *Langmuir* 24:6409–6413.
32. Perreault F, de Faria AF, Nejati S, Elimelech M (2015) Antimicrobial properties of graphene oxide nanosheets: Why size matters. *ACS Nano* 9:7226–7236.
33. Pasquini LM, Hashmi SM, Sommer TJ, Elimelech M, Zimmerman JB (2012) Impact of surface functionalization on bacterial cytotoxicity of single-walled carbon nanotubes. *Environ Sci Technol* 46:6297–6305.
34. Liu C, Faria AF, Ma J, Elimelech M (2017) Mitigation of biofilm development on thin-film composite membranes functionalized with zwitterionic polymers and silver nanoparticles. *Environ Sci Technol* 51:182–191.
35. Montheard JP, Chatzopoulos M, Chappard D (1992) 2-Hydroxyethyl methacrylate (HEMA): Chemical properties and applications in biomedical fields. *J Macromol Sci Polym Rev* 32:1–34.
36. Zou X, Zhang L, Wang Z, Luo Y (2016) Mechanisms of the antimicrobial activities of graphene materials. *J Am Chem Soc* 138:2064–2077.
37. Wang Z, et al. (2016) Biological and environmental interactions of emerging two-dimensional nanomaterials. *Chem Soc Rev* 45:1750–1780.
38. Perreault F, Fonseca de Faria A, Elimelech M (2015) Environmental applications of graphene-based nanomaterials. *Chem Soc Rev* 44:5861–5896.
39. Zhou R, Gao H (2014) Cytotoxicity of graphene: Recent advances and future perspective. *Wiley Interdiscip Rev Nanomed Nanobiotechnol* 6:452–474.
40. Chen KL, Bothun GD (2014) Nanoparticles meet cell membranes: Probing nonspecific interactions using model membranes. *Environ Sci Technol* 48:873–880.
41. Verkman AS (1995) Optical methods to measure membrane transport processes. *J Membr Biol* 148:99–110.
42. Lis M, et al. (2011) The effect of lipid oxidation on the water permeability of phospholipids bilayers. *Phys Chem Chem Phys* 13:17555–17563.
43. Kozhevnikov IV (1998) Catalysis by heteropoly acids and multicomponent polyoxometalates in liquid-phase reactions. *Chem Rev* 98:171–198.
44. Vecitis CD, Zodrow KR, Kang S, Elimelech M (2010) Electronic-structure-dependent bacterial cytotoxicity of single-walled carbon nanotubes. *ACS Nano* 4:5471–5479.
45. Buxton GV, Greenstock CL, Helman WP, Ross AB (1988) Critical review of rate constants for reactions of hydrated electrons, hydrogen atoms and hydroxyl radicals ($\cdot OH/\cdot O^-$) in aqueous solution. *J Phys Chem Ref Data* 17:513–886.
46. Gurunathan S, et al. (2013) Antibacterial activity of dithiothreitol reduced graphene oxide. *J Ind Eng Chem* 19:1280–1288.
47. Gurunathan S, Han JW, Dayem AA, Eppakayala V, Kim JH (2012) Oxidative stress-mediated antibacterial activity of graphene oxide and reduced graphene oxide in Pseudomonas aeruginosa. *Int J Nanomedicine* 7:5901–5914.
48. Sanchez VC, Jachak A, Hurt RH, Kane AB (2012) Biological interactions of graphene-family nanomaterials: An interdisciplinary review. *Chem Res Toxicol* 25:15–34.
49. Fahey RC, Brown WC, Adams WB, Worsham MB (1978) Occurrence of glutathione in bacteria. *J Bacteriol* 133:1126–1129.
50. Winterbourn CC, Metodiewa D (1999) Reactivity of biologically important thiol compounds with superoxide and hydrogen peroxide. *Free Radic Biol Med* 27:322–328.
51. Carmel-Harel O, Storz G (2000) Roles of the glutathione- and thioredoxin-dependent reduction systems in the Escherichia coli and saccharomyces cerevisiae responses to oxidative stress. *Annu Rev Microbiol* 54:439–461.
52. Lyon DY, Alvarez PJJ (2008) Fullerene water suspension (nC60) exerts antibacterial effects via ROS-independent protein oxidation. *Environ Sci Technol* 42:8127–8132.
53. Moghadam BY, Hou W-C, Corredor C, Westerhoff P, Posner JD (2012) Role of nanoparticle surface functionality in the disruption of model cell membranes. *Langmuir* 28:16318–16326.
54. Akhavan O, Ghaderi E, Esfandiar A (2011) Wrapping bacteria by graphene nanosheets for isolation from environment, reactivation by sonication, and inactivation by near-infrared irradiation. *J Phys Chem B* 115:6279–6288.